





## Large-scale and small-scale contribution to the skin friction reduction in a modified turbulent boundary layer by a large-eddy break-up device

C. I. Chan <sup>1,\*</sup>, R. Örlü <sup>2</sup>, P. Schlatter <sup>2</sup> and R. C. Chin <sup>1</sup>

<sup>1</sup>*School of Mechanical Engineering, University of Adelaide, South Australia 5005, Australia*

<sup>2</sup>*SimEx/FLOW, Engineering Mechanics, KTH Royal Institute of Technology, SE-100 44 Stockholm, Sweden*



(Received 27 September 2021; accepted 14 February 2022; published 15 March 2022)

The role of streamwise length scales ( $\lambda_x$ ) in turbulent skin friction generation is investigated using a direct numerical simulation data set of an incompressible zero pressure gradient turbulent boundary layer and the spectral analysis based on the Fukagata-Iwamoto-Kasagi (FIK) identity by Fukagata *et al.* [K. Fukagata *et al.*, *Phys. Fluids* **14**, L73 (2002)]. The total skin friction generation associated with motions scaled with local boundary layer thickness  $\delta$  of  $\lambda_x < 3\delta$  and  $\lambda_x > 3\delta$  is assessed. The FIK-identity-based spectral analysis is further extended to include the quadrant analysis of Reynolds shear stress. This allows one to relate the turbulent skin friction generation to the quadrant events of Reynolds shear stress, which plays a central role in the momentum transport in turbulent wall-bounded flows. The small-scale ejection and sweep events ( $\lambda_x < 3\delta$ ) contribute to a significant portion of turbulent skin friction. However, it is found that the large-scale ejection and sweep events with streamwise length scales at  $\lambda_x > 3\delta$  are equally important. The turbulent skin friction reduction associated with the modification of large- and small-scale quadrant events is studied, using well-resolved simulation data sets of a large-eddy break-up (LEBU) device in a turbulent boundary layer. The results reveal that LEBUs modify both the large- and small-scale ejection and sweep events, yielding a substantial turbulent skin friction reduction.

DOI: [10.1103/PhysRevFluids.7.034601](https://doi.org/10.1103/PhysRevFluids.7.034601)

### I. INTRODUCTION

A theoretical and practical important feature in the turbulent boundary layer (TBL) is the mean wall-shear stress, defined as the mean streamwise velocity gradient in the wall-normal direction at the wall. This wall quantity provides the relevant velocity and length scales for viscous scaling. For practical purposes, the control of skin friction drag is important for engineering applications involving fluid flows on a solid surface. Understanding the flow dynamics related to the skin friction generation mechanism is essential to provide insights into optimizing flow control strategies.

The wall-shear stress is known to be associated with different scales of coherent structures from the near-wall region to the outer region. In the near-wall region, coherent structures are composed of quasistreamwise vortices and streamwise elongated low- and high-speed streaks [1–3]. The low-speed streaks (ejections) lift up from the wall by bursting, and they account for 70% of the Reynolds shear stress generation and play an essential role in the production of turbulent kinetic energy [4–7]. The ejection events are subsequently followed by relatively larger-scale and faster-moving sweep events that occur closer to the wall [8]. The near-wall turbulence was further characterized by the quadrant analysis of Reynolds shear stress [9]. An ejection event is related to the  $Q2$  motion, defined as  $u < 0$  and  $v > 0$ , where  $u$ ,  $v$  are the velocity fluctuations in the streamwise and wall-normal

\*chiip.chan@adelaide.edu.au

direction, and a sweep event is related to the  $Q4$  motion (where  $u > 0$ ,  $v < 0$ ). The  $Q2$  and  $Q4$  motions were shown to be significant contributions to the mean shear stress [9].

In the logarithmic and outer regions, the large-scale motions (LSMs) and very-large-scale motions (VLSMs) that scale with local boundary layer thickness ( $\delta$ ), channel half height ( $h$ ), or the pipe radius ( $r$ ) [10–14] carry considerable fractions of the mean Reynolds shear stress and turbulent kinetic energy [15,16], and they play a crucial role in turbulence production. At sufficiently high Reynolds numbers, their footprints extend to the wall as the low wave-number energy shift in the streamwise velocity energy spectra and the large-scale influence on the small-scale structures can be expressed as amplitude modulation [14,17,18]. The large-scale motions have also been known to affect the wall-shear stress [19–21].

Given the established link between the wall-shear stress and the different scales of motions across the TBL, the contribution of turbulent coherent structures to the total skin friction [ $C_f = 2\tau_w/(\rho U_\infty^2)$ , where  $\tau_w$ ,  $\rho$ , and  $U_\infty$  are the mean wall-shear stress, fluid density and free-stream velocity, respectively] has been investigated through different approaches. Fukagata *et al.* [22] proposed a mathematical relation between the turbulent skin friction and the Reynolds shear stress distribution across the boundary layer, based on the mean momentum equation [referred to as the Fukagata-Iwamoto-Kasagi (FIK) identity]. Subsequently, Renard and Deck (RD) [23] proposed an alternative skin friction decomposition based on the streamwise kinetic energy transport equation, referred to as the RD identity, which links the skin friction generation to the turbulent kinetic energy production, dissipation, and viscous transport, obtained in a reference frame moving with respect to the wall (absolute reference frame). Yoon *et al.* [24] presented a novel approach based on the mean vorticity transport equation. The contribution of large-scale vortical motions to the skin friction was calculated utilizing co-spectra of velocity-vorticity correlations associated with vorticity lifting and vortex stretching [24–27]. These three mean wall-shear stress decomposition methods that derived from the mean momentum, energy, and vorticity equations have been utilized in wall-bounded turbulent shear flows for different research purposes (e.g., analysis of drag reduced flows).

Among the studies using the FIK identity, Deck *et al.* [28] investigated the turbulent skin friction contribution of the large-scale structures above the near-wall region in a TBL at moderate to high Reynolds numbers. By scale decomposition of the turbulent contribution in the streamwise direction, the turbulent skin friction generations associated with small- and large-scale motions were calculated. The study revealed that a significant portion of total skin friction (>50%) is generated by the large scales at  $\lambda_x > \delta$  (where  $\lambda_x$  is the streamwise length scale). Similar conclusions were recently drawn in closed and open channel flows for large scales at  $\lambda_x > 3h$ , at friction Reynolds number up to  $Re_\tau \simeq 2400$  [29]. Here, the friction Reynolds number is defined as  $Re_\tau = \delta u_\tau/\nu$  or  $hu_\tau/\nu$ , where  $u_\tau = \sqrt{\tau_w/\rho}$  is the friction velocity and  $\nu$  is the kinematic viscosity. The large-scale influence on the turbulent skin friction in the spanwise direction was examined by de Giovanetti *et al.* [30] for channel flows, where the skin friction generation associated with the energy-containing motions [21], based on the method of Deck *et al.* [28], was assessed for the spanwise wave number. The very-large-scale motions at  $\lambda_z > 1.5h$  and their relevant interactions with energy-containing motions at smaller scales were shown to account for about 20–30% of total skin friction at  $Re_\tau \simeq 2000$  [30].

Recent studies have also examined the turbulent skin friction generation in the framework of quadrant analysis of Reynolds shear stress [31,32]. In the classical view of the hairpin-vortex paradigm, the organization of wall-bounded turbulent flow is composed of pairing or growth of the hairpin vortices [33], and the sweep and ejection events are often considered to be related to the spatial organization of the hairpin-vortex signature [2,7]. An alternative explanation to the hairpin-packet paradigm is that the three-dimensional structures responsible for the momentum transport can be studied in terms of the wall-detached and attached groups of structures [34,35]. The detached groups are composed of small and isotropically oriented structures and they have almost no contribution to the mean Reynolds shear stress. The attached groups contribute to the mean Reynolds shear stress. In the logarithmic region, the ensemble-averaged structure commonly

forms a side-by-side sweep and ejection pair partitioned by a quasistreamwise vortex. The large-scale attached structures that extend from the wall into the logarithmic layer have relatively long lifetimes and are roughly self-similar in spatial extent, and the intense negative Reynolds shear stress events are responsible for most of the vertical momentum transport [34–36]. It is evident that the mechanism responsible for generating wall-shear stress can be linked to the existence of coherent motions that constitute the ejection and sweep events. Their statistical contributions to the turbulent skin friction were calculated based on their wall-normal distributions [31,32], where the  $Q2$  and  $Q4$  motions were involved in substantial amounts of turbulent skin friction and equal to 40–50% of the total skin friction, respectively.

Decades before the establishment of the role that the large-scale structures play in wall-bounded turbulence and their influence on the near-wall region, so-called outerlayer devices or large-eddy break-up (LEBU) devices with the aim to destroy large coherent structures, attracted the interest of the community [37–39]. These devices usually consist of one or more thin plates or airfoils placed parallel to the wall and immersed in the outer region of a turbulent boundary layer. While initial work claimed to have found a passive control mechanism that would yield not only local skin friction reduction but also net drag reduction, these promising results could never be replicated through direct drag measurements in towing tanks [40,41], i.e., no net drag reduction was obtained. These results were recently also confirmed through direct numerical simulations (DNS) [31,42] at low Reynolds numbers and well-resolved large eddy simulations (LES) in large domain size (in particular streamwise) at Reynolds numbers that match some of the low Reynolds number wind-tunnel experiments [32,43]. Despite the established result that no net drag reduction is possible, there remains interest in the community to understand the underlying mechanism for the local skin friction reduction that is sustainable up to  $O(100\delta)$ . Hence, LEBUs remain of interest, e.g., they can be used to reduce optical distortions when viewing through a turbulent boundary layer by decreasing the intermittency in the outer portion of the boundary layer [44] or to reduce the pressure fluctuations at the wall by destroying at least part of the large-scale structures and thereby decreasing the induced noise, e.g., for airplane travel [42].

The objective of the present paper is to explore the turbulent skin friction generation in canonical TBLs and TBLs modified by LEBUs using an approach that incorporates two approaches: (i) the scale decomposition for the FIK identity that characterizes the scale-by-scale contributions to turbulent skin friction [28], and (ii) the quadrant decomposition that characterizes the turbulent skin friction contribution of each quadrant of the Reynolds shear stress [31,32]. This paper is also an extension of the authors' previous work [32]; in particular, well-resolved LES data sets of TBLs modified by LEBU devices are analyzed based on the approach presented here. The LEBUs were set up at different wall-normal heights in the flow: (i) near-wall region ( $0.1\delta$ ) and (ii) outer region ( $0.5\delta$  and  $0.8\delta$ ), which targeted different flow regions and resulted in varying degrees of skin friction reduction and attenuation of the Reynolds shear stress contribution downstream of the LEBU. The LEBU data sets serve as good candidates for the investigation of the large- and small-scale quadrant events and their relationship to the wall-shear stress generation, under the manipulations of LEBUs. The remainder of this paper is organized as follows. In Sec. II, we first introduce the numerical code and data sets. The approach quantifying turbulent skin friction generation by the quadrant events is introduced in Sec. III. In Sec. IV, the results of the LEBU flows compared to the DNS of an unmanipulated spatially evolving TBL and discussions are presented. This is followed by some concluding remarks in Sec. V.

## II. SIMULATION DATA SETS

### LES LEBU and DNS TBL data sets

In the following, the streamwise, wall-normal, and spanwise coordinates are denoted as  $\mathbf{x} = (x, y, z)$  or  $x_i$ , and the instantaneous (resolved) velocity components are denoted as  $\hat{\mathbf{u}} = (\hat{u}, \hat{v}, \hat{w})$  or  $\hat{u}_i$ , respectively. The streamwise, wall-normal, and spanwise velocity fluctuations are denoted

TABLE I. LEBU parameters for the three LEBU cases.  $x/\delta_0^*$  and  $y/\delta$  denote the local streamwise and wall-normal locations of the LEBU, respectively.  $\delta_0^*$  is the inlet displacement thickness which gives  $\text{Re}_{\delta_0^*} = U_\infty \delta_0^* / \nu = 450$ .  $l_x$  and  $l_y$  denote the LEBU blade length and thickness, respectively.  $\delta$  is the local boundary layer thickness.

| LEBU case | $x/\delta_0^*$ | $y/\delta$ | $l_x/\delta_0^*$ | $l_y/\delta_0^*$ | $\delta^+$ | $\delta/\delta_0^*$ |
|-----------|----------------|------------|------------------|------------------|------------|---------------------|
| LB-01     | 1000           | 0.1        | 20               | 0.17             | 450        | 22.3                |
| LB-05     | 1000           | 0.5        | 20               | 0.17             | 450        | 22.3                |
| LB-08     | 1000           | 0.8        | 20               | 0.17             | 450        | 22.3                |

as  $\mathbf{u} = (u, v, w)$  or  $u_i$ , respectively. A capital letter denotes the spanwise and temporal-averaged velocity component and the symbol  $\langle \cdot \rangle$  denotes the spanwise and temporal-averaged quantity (i.e.,  $\mathbf{U} = \langle \hat{\mathbf{u}} \rangle$  and  $\hat{\mathbf{u}} = \mathbf{U} + \mathbf{u}$ ). Quantities scaled by an inner unit are denoted by the superscript  $+$ . Three LEBU LES were performed using a fully spectral numerical code [45]. The code is two-dimensional (2D) parallelized running on  $O(10^3)$  processors [46]. A sub-grid-scale approximate deconvolution model-relaxation term (ADM-RT) is employed to compute approximations to the unfiltered solutions by a repeated filter operation [47,48]. The governing equations are the resolved incompressible continuity and Navier-Stokes equations:

$$\frac{\partial \hat{u}_i}{\partial x_i} = 0, \quad (1)$$

$$\frac{\partial \hat{u}_i}{\partial t} + \hat{u}_j \frac{\partial \hat{u}_i}{\partial x_j} + \frac{\partial \hat{p}}{\partial x_i} - \frac{1}{\text{Re}} \frac{\partial^2 \hat{u}_i}{\partial x_j \partial x_j} = -\chi H_N \otimes \hat{u}_i, \quad (2)$$

where  $\hat{p}$  refers to the instantaneous (resolved) pressure and  $\otimes$  denotes the convolution. The relaxation term  $-\chi H_N \otimes \hat{u}_i$ :  $\chi$  is the model coefficient;  $H_N \otimes \hat{u}_i$  are the high-pass, approximately deconvolved quantities where  $H_N := (I - G)^{N+1}$  is the high-pass filter;  $G$ ,  $N$ , and  $I$  are the low-pass filter, deconvolution order, and identity operator, respectively. Detailed descriptions can be found in Schlatter *et al.* [48]. The spatial discretization is based on a Fourier series with 3/2 zero padding for de-aliasing in the streamwise and spanwise directions, and a Chebyshev polynomial is employed in the wall-normal direction. The time advancement is carried out by a second-order Crank-Nicolson scheme for the viscous terms and a third-order four-stage Runge-Kutta scheme for the nonlinear terms [45]. A low-amplitude volume force trip is applied to the Navier-Stokes equations at the region very close to the inlet to trigger a rapid transition to turbulent flow. For further details on the tripping methods, the reader is referred to Schlatter and Örlü [49]. To retain periodic boundary conditions in the streamwise direction, a fringe region is employed at the downstream of the flow, close to the end of the computational domain. In the fringe region, the flow is damped via a volume force until it returns to the inflow condition [45,50].

The LEBU used in this study is a thin blade type in single plate arrangement and is introduced by an immersed boundary method [51]. A volume force is computed and imposed to the governing equations to ensure that the velocities within the grid points in the LEBU reduce to zero [43]. The LEBU is positioned at streamwise location  $x/\delta_0^* = 1000$  from the inlet, and corresponds to local friction Reynolds number  $\text{Re}_\tau = \delta^+ \approx 450$ , where  $\delta_0^*$  is the inlet displacement thickness. For the three LEBU cases, the LEBU is placed at  $y/\delta = 0.1, 0.5,$  and  $0.8$ , respectively. Hereafter, the three cases are referred to as LB-01, LB-05, and LB-08, respectively. The LEBU parameters that scale with the inlet displacement thickness are, respectively,  $l_x \approx 20$  for the blade length and  $l_y \approx 0.17$  for the blade thickness, and the LEBU is assumed to be spanwise homogeneous. A summary of the LEBU parameters is given in Table I. The LEBU LES data sets have been validated in a previous study [32]. For each TBL with LEBU device, time series statistics are collected and evaluated at two friction Reynolds numbers,  $\text{Re}_\tau \simeq 500$  and  $1000$ . For comparison, a DNS TBL data set at  $\text{Re}_\tau \simeq 500$  and  $1000$  is used to represent an unmanipulated zero-pressure-gradient (ZPG) TBL [52],

TABLE II. Simulation parameters for the computational domains of DNS TBL [52] and LES LEBU in TBL.  $Re_\tau$  is the local friction Reynolds number.  $L_x$ ,  $L_y$ , and  $L_z$  are the computational domain sizes along the streamwise, wall-normal, and spanwise directions, respectively.  $N_x$ ,  $N_y$ , and  $N_z$  are the spectral collocation points.  $\Delta x^+$ ,  $\Delta y^+$ , and  $\Delta z^+$  denote the grid spacings in viscous units.

| Case  | $Re_\tau$ | $(L_x \times L_y \times L_z)/\delta_0^*$ | $N_x \times N_y \times N_z$    | $\Delta x^+$ | $\Delta(y_{\min}^+, y_{\max}^+)$ | $\Delta z^+$ |
|-------|-----------|--|--------------------------------|--------------|----------------------------------|--------------|
| DNS   | 520, 990  | $10000 \times 300 \times 360$            | $12800 \times 769 \times 1024$ | 8.6          | (0.02, 10.0)                     | 3.9          |
| LB-01 | 520, 1020 | $6000 \times 200 \times 240$             | $6144 \times 513 \times 512$   | 11.2         | (0.03, 10.6)                     | 5.4          |
| LB-05 | 480, 1000 | $6000 \times 200 \times 240$             | $6144 \times 513 \times 512$   | 11.2         | (0.03, 10.6)                     | 5.4          |
| LB-08 | 530, 990  | $6000 \times 200 \times 240$             | $6144 \times 513 \times 512$   | 11.2         | (0.03, 10.6)                     | 5.4          |

and is referred to as the reference case (hereafter referred to as DNS). The detailed parameters of all data sets used in the present study are summarized in Table II. Figure 1 compares the mean velocity profiles and fluctuations of the present LEBU LES at  $Re_\tau \simeq 500$  and  $Re_\tau \simeq 1000$  with those from the reference DNS, which collapse reasonably well at  $Re_\tau \simeq 1000$ , thereby suggesting that the LEBU effects have almost vanished and the flow statistics converged to the one of the DNS.

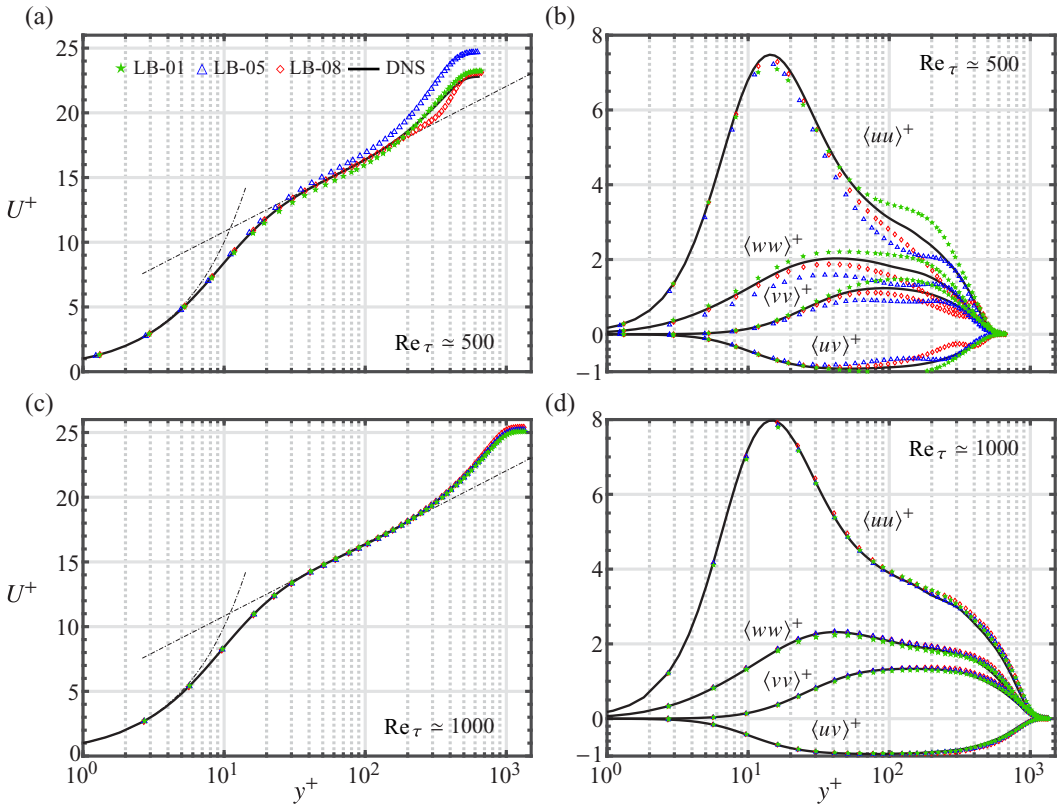


FIG. 1. Mean velocity profile  $U^+$ , Reynolds normal stresses  $\langle uu \rangle^+$ ,  $\langle vv \rangle^+$ , and  $\langle ww \rangle^+$ , and Reynolds shear stress  $\langle uv \rangle^+$  at (a),(b)  $Re_\tau \simeq 500$  and (c),(d)  $Re_\tau \simeq 1000$ . Dash-dotted lines in (a) and (c) represent the linear and logarithmic-law regions  $1/\kappa \ln(y^+) + B$  with  $\kappa = 0.41$  and  $B = 5.2$ .

TABLE III. Flow conditions for the simulations of ZPG TBL: DNS TBL (DNS) and LEBU LES (LB-01, LB-05, and LB-08).  $Re_\theta = \theta U_\infty / \nu$  is the Reynolds number based on the momentum thickness ( $\theta$ ) and  $Re_\delta^* = \delta^* U_\infty / \nu$  is the Reynolds number based on the displacement thickness ( $\delta^*$ ).  $C_f$  and  $C_{f,2}$  denote the total skin friction and the turbulent skin friction coefficients following relation (3), respectively.

| Case  | $Re_\tau$ | $Re_\theta$ | $Re_\delta^*$ | $C_f$   | $C_{f,2}$ | $C_{f,2}/C_f(\%)$ |
|-------|-----------|-------------|---------------|---------|-----------|-------------------|
| DNS   | 520       | 1470        | 2110          | 0.00383 | 0.00266   | 69.3              |
|       | 990       | 3090        | 4320          | 0.00318 | 0.00232   | 73.2              |
| LB-01 | 520       | 1610        | 2340          | 0.00369 | 0.00294   | 79.7              |
|       | 1020      | 3180        | 4430          | 0.00317 | 0.00234   | 73.8              |
| LB-05 | 480       | 1610        | 2400          | 0.00327 | 0.00204   | 62.5              |
|       | 1000      | 3170        | 4450          | 0.00314 | 0.00238   | 75.6              |
| LB-08 | 530       | 1720        | 2450          | 0.00373 | 0.00207   | 55.6              |
|       | 990       | 3210        | 4500          | 0.00309 | 0.00238   | 76.9              |

### III. METHODOLOGY

#### Quadrant decomposition of the turbulent skin friction

The streamwise-spectral form of the turbulent skin friction was proposed by Deck *et al.* [28] based on the FIK decomposition of the total skin friction coefficient (i.e.,  $C_f$ ) first introduced in Fukagata *et al.* [22]. The FIK decomposition of  $C_f$  is given by the triple integration of the mean streamwise momentum equation over the wall-normal direction, where the resulting equation yields

$$\begin{aligned}
 C_f = & \underbrace{\frac{4(1 - \delta^*/\delta)}{Re_\delta}}_{C_{f,1}} + \underbrace{\int_0^1 \frac{4(1 - y/\delta)}{U_\infty^2} (-\langle uv \rangle) d(y/\delta)}_{C_{f,2}} \\
 & + \underbrace{\int_0^1 \frac{4(1 - y/\delta)}{U_\infty^2} (-UV) d(y/\delta) - \int_0^1 \frac{2\delta(1 - y/\delta)^2}{U_\infty^2} \left( \frac{\partial U^2}{\partial x} + \frac{\partial \langle uu \rangle}{\partial x} - \nu \frac{\partial^2 U}{\partial x^2} \right) d(y/\delta)}_{C_{f,3}}.
 \end{aligned} \tag{3}$$

The  $C_{f,1}$  and  $C_{f,2}$  denote the ‘‘laminar’’ and ‘‘turbulent’’ contributions, respectively. The term  $C_{f,3}$  is associated with the mean flow convection and spatial development. Table III lists the total and turbulent skin friction coefficients. The turbulent skin friction coefficient (i.e.,  $C_{f,2}$ ) can be written in spectral form by introducing the co-spectrum of the Reynolds shear stress,

$$\Phi_{-uv}(k_x) = U_c \Phi_{-uv}(f), \quad k_x = 2\pi f / U_c, \quad -\langle uv \rangle = \int_0^\infty \Phi_{-uv}(k_x) dk_x, \tag{4}$$

$$C_{f,2} = \int_0^1 \underbrace{\frac{4(1 - y/\delta)}{U_\infty^2} (-\langle uv \rangle)}_{F_R} d(y/\delta) = \int_0^1 \int_0^\infty \underbrace{\frac{4(1 - y/\delta)}{U_\infty^2} (\Phi_{-uv})}_{\Phi_{F_R}} d(k_x) d(y/\delta), \tag{5}$$

where the streamwise co-spectrum is approximated by the frequency spectrum and Taylor’s frozen field hypothesis. In this context, the selection of the convection velocity is crucial and has been extensively studied [53,54]. For the present analysis, the commonly preferred choice of setting it equal to the local mean velocity,  $U_c(y) = U(y)$ , is utilized, which has been shown to be suitable for turbulent boundary layers [54]. The spectral form of the turbulent skin friction is thus represented by the co-spectrum  $\Phi_{F_R}$  (integrand). The large-scale and small-scale Reynolds shear stress components

based on a streamwise cutoff wave number ( $k_{x,c}$ ) can be expressed as

$$-\langle u^L v^L \rangle = \int_0^{k_{x,c}} \Phi_{-uv}(k_x) dk_x, \quad -\langle u^S v^S \rangle = \int_{k_{x,c}}^{\infty} \Phi_{-uv}(k_x) dk_x, \quad (6)$$

and the wall-normal distribution of large scales  $F_L^R$  and small scales  $F_S^R$  to the turbulent skin friction can be expressed as

$$C_{f,2} = \int_0^1 \left[ \underbrace{\int_0^{k_{x,c}} \frac{4(1-y/\delta)}{U_\infty^2} (\Phi_{-uv}) d(k_x)}_{F_L^R} \right] + \left[ \underbrace{\int_{k_{x,c}}^{\infty} \frac{4(1-y/\delta)}{U_\infty^2} (\Phi_{-uv}) d(k_x)}_{F_S^R} \right] d(y/\delta). \quad (7)$$

Similarly, the large-scale and small-scale velocity fluctuations can be first computed in Fourier space at a constant cutoff wave number  $k_x = k_{x,c}$ :

$$u_i(\mathbf{x}, t) = u_i^L(k_{x,c}, \mathbf{x}, t) + u_i^S(k_{x,c}, \mathbf{x}, t). \quad (8)$$

The large-scale and small-scale components of the Reynolds shear stress satisfy

$$\langle uv \rangle(y) = \langle u^L v^L \rangle(k_{x,c}, y) + \langle u^S v^S \rangle(k_{x,c}, y), \quad (9)$$

where (9) is the large- and small-scale Reynolds shear stress obtained in (6) (refer to the Appendix). The quadrant decomposition of the Reynolds shear stress and the integrand  $F_R$  in (5) can be written as

$$-\langle uv \rangle = \sum_{n=1}^4 -\langle uv \rangle^{Q_n}, \quad F_R = \sum_{n=1}^4 f_R^{Q_n} = \frac{4(1-y/\delta)}{U_\infty^2} \left[ \sum_{n=1}^4 -\langle uv \rangle^{Q_n} \right], \quad (10)$$

where  $Q_n$  denotes the  $n$ th quadrant [55]. The skin friction coefficient generated by each quadrant of Reynolds shear stress can be obtained by integrating (10) over the wall-normal direction,

$$C_{f,2}^{Q_n} = \int_0^1 f_R^{Q_n} d(y/\delta), \quad (11)$$

where, for instance, the Reynolds shear stress in the second quadrant ( $Q2$ ) is defined as  $-\langle uv \rangle^{Q2} = -\langle uv | (u < 0, v > 0) \rangle$ . The scale-by-scale quadrant decomposition is defined using (8), (9), and the following criterion, e.g., for  $Q2$  ( $n = 2$ ):

$$\begin{aligned} -\langle u^L v^L \rangle^{Q2} &= -\langle u^L v^L | (u < 0, v > 0) \rangle, & -\langle u^S v^S \rangle^{Q2} &= -\langle u^S v^S | (u < 0, v > 0) \rangle, \\ -\langle u^L v^S \rangle^{Q2} &= -\langle u^L v^S | (u < 0, v > 0) \rangle, & -\langle u^S v^L \rangle^{Q2} &= -\langle u^S v^L | (u < 0, v > 0) \rangle, \end{aligned} \quad (12)$$

where the scale-by-scale velocity components are obtained for large-scale ( $L$ ), small-scale ( $S$ ), and large- and small-scale interactions ( $LS$  and  $SL$ ). The velocity components satisfy

$$\begin{aligned} -\langle u^L v^L \rangle &= \sum_{n=1}^4 -\langle u^L v^L \rangle^{Q_n}, \\ -\langle u^S v^S \rangle &= \sum_{n=1}^4 -\langle u^S v^S \rangle^{Q_n}, \\ -\langle u^L v^S \rangle &= \sum_{n=1}^4 -\langle u^L v^S \rangle^{Q_n} = 0, \\ -\langle u^S v^L \rangle &= \sum_{n=1}^4 -\langle u^S v^L \rangle^{Q_n} = 0. \end{aligned} \quad (13)$$



Substituting the criterion (13) into  $-\langle uv \rangle^{Q_n}$  of the integrand  $F_R$  in (10) leads to

$$\begin{aligned}
 F_R^L &= \sum_{n=1}^4 f_R^{L,Q_n} = \frac{4(1-y/\delta)}{U_\infty^2} \left[ \sum_{n=1}^4 -\langle u^L v^L \rangle^{Q_n} \right], \\
 F_R^S &= \sum_{n=1}^4 f_R^{S,Q_n} = \frac{4(1-y/\delta)}{U_\infty^2} \left[ \sum_{n=1}^4 -\langle u^S v^S \rangle^{Q_n} \right], \\
 F_R^{LS} &= \sum_{n=1}^4 f_R^{LS,Q_n} = \frac{4(1-y/\delta)}{U_\infty^2} \left[ \sum_{n=1}^4 -\langle u^L v^S \rangle^{Q_n} \right] = 0, \\
 F_R^{SL} &= \sum_{n=1}^4 f_R^{SL,Q_n} = \frac{4(1-y/\delta)}{U_\infty^2} \left[ \sum_{n=1}^4 -\langle u^S v^L \rangle^{Q_n} \right] = 0,
 \end{aligned} \tag{14}$$

and thus the integrand  $F_R$  can be represented by

$$F_R = \sum_{n=1}^4 f_R^{L,Q_n} + \sum_{n=1}^4 f_R^{S,Q_n}, \tag{15}$$

and the integrand groups in (15) yield the skin friction coefficient generated by different streamwise scales of quadrant events:

$$C_{f,2}^{L,Q_n} = \int_0^1 f_R^{L,Q_n} d(y/\delta), \quad C_{f,2}^{S,Q_n} = \int_0^1 f_R^{S,Q_n} d(y/\delta). \tag{16}$$

A cutoff wavelength  $\lambda_{x,c} = 3\delta$  is used in the present study. The term large-scale motion defined here refers to streamwise length scales of  $\lambda_x > 3\delta$  and the small-scale motion defines streamwise length scales of  $\lambda_x < 3\delta$ . The cutoff wavelength is based on the literature as follows: (i) the large-scale motions correspond to the streamwise scales with orders of the commonly observed Reynolds dependent LSMs [ $\lambda_x \sim O(3\delta)$ ] and VLSMs [ $\lambda_x \sim O(10\delta)$ ] in wall-bounded flows [10,14–17,33,56]; and (ii) the small-scale motions consist of the Reynolds independent near-wall streaks with a typical streamwise scale of  $\lambda_x^+ \simeq 1000$  [3]. It must be pointed out that a limitation of the present study is that the Reynolds numbers considered here might be too low to observe a distinct scale separation between small- and large-scale motions [17], in which case the results based on the “large scales” and “small scales” here might not be conclusive for relatively high Reynolds numbers.

## IV. RESULTS

### A. Streamwise length scales associated with turbulent skin friction generation

The total skin friction generation associated with motions at a cutoff wavelength  $\lambda_{x,c} = 3\delta$  is first assessed using the FIK identity. The premultiplied  $\Phi_{F_R}$  in (5) is shown in Fig. 2. For the DNS case at  $\text{Re}_\tau \simeq 500$  [Fig. 2(a)], the energy appears to center around  $\lambda_x \simeq 2\delta$ ,  $y \simeq 0.35\delta$  [marked with dotted lines in Fig. 2(a)]. The streamwise scales of  $\lambda_x > 3\delta$  are responsible for 29% of the total skin friction coefficient [Fig. 2(a)], and they account for 27% at  $\text{Re}_\tau \simeq 1000$  [Fig. 2(e)]. The values are comparable with that reported by de Giovanetti *et al.* [30] who found that the motions at  $\lambda_\tau \geq 1.5h$  were responsible for 25–30% total skin friction generation in channel flows at  $\text{Re}_\tau \simeq 2000$ . Figures 2(a) and 2(e) are also consistent with the results in Duan *et al.* [29], who reported that the maximum contribution to  $C_f$  resides within  $y/h \simeq 0.3$ – $0.4$  in open and closed channels, thus suggesting that the wall-normal location in which the most amount of  $C_{f,2}$  resided seems to globally scale with the outer length scale. For the LB-01 case, shown in Fig. 2(b), the increase in  $\Phi_{F_R}$  at  $\text{Re}_\tau \simeq 500$  reflects the regeneration of Reynolds shear stress, as discussed in Ref. [32]. Interestingly, not only do the smaller-scale motions at  $\lambda_x < 3\delta$  increase, but also the motions  $\lambda_x > 3\delta$  within



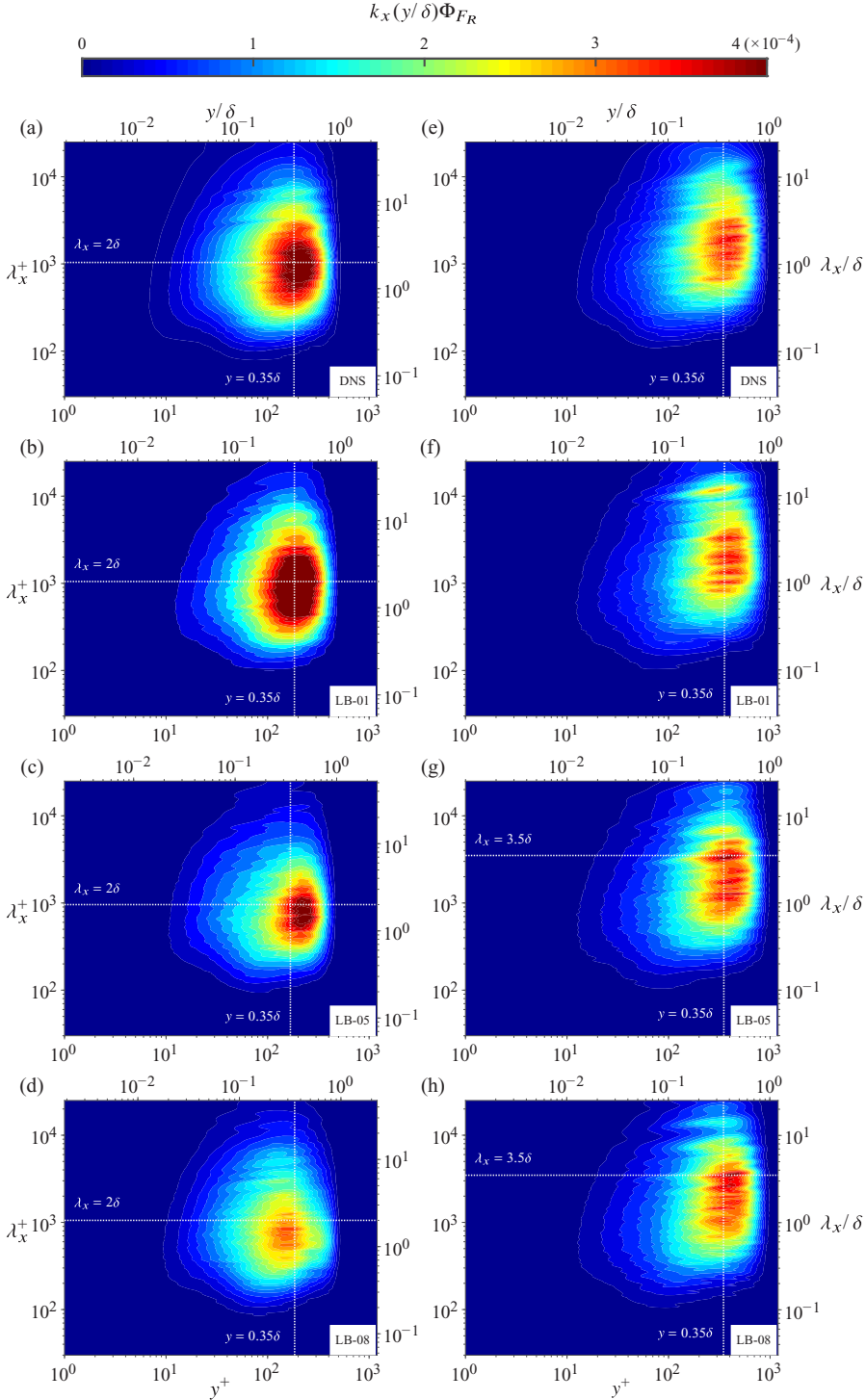


FIG. 2. Streamwise premultiplied scale-by-scale contribution  $k_x(y/\delta)\Phi_{FR}$  to the turbulent skin friction coefficient  $C_{f,2}$  based on (5) for (a),(e) DNS, (b),(f) LB-01, (c),(g) LB-05, and (d),(h) LB-08, at (a)–(d)  $Re_\tau \simeq 500$  and (e)–(h)  $Re_\tau \simeq 1000$ . Dashed white lines mark the features discussed in Sec. IV A.

region  $y/\delta \simeq 0.1\text{--}0.8$  are found to be larger. When comparing the LB-05 and LB-08 to the DNS [Figs. 2(c) and 2(d)], it is seen that the larger-scale energy ( $\lambda_x > 2\delta$ ) that is observed in DNS is reduced and is partly transferred to smaller scales ( $\lambda_x < 2\delta$ ) and to a higher  $y/\delta$ . This is consistent with the large-scale break-up effect as observed for spanwise length scales [43], which is likely due to the break up of the large-scale momentum bulges into small-scale turbulence downstream of the LEBU. The majority of turbulent skin friction generation is extended to larger  $\lambda_x^+$ , up to  $\lambda_x^+ \sim 10^4$  at  $\text{Re}_\tau \simeq 1000$  in the DNS case shown in Fig. 2(e). The long-term influence of the LEBU device on the turbulent structures is shown in Figs. 2(f)–2(h). In particular for the LB-05 and LB-08 cases, more energy resides within  $\lambda_x/\delta \simeq 3\text{--}4$  and  $y/\delta \simeq 0.3\text{--}0.4$  [marked with white dotted lines in Figs. 2(g) and 2(h)] compared with the DNS, indicating the growing significance of the large-scale motions [ $\lambda_x \sim O(\delta)$ ] to  $C_{f,2}$  in the outer region within  $y/\delta \simeq 0.3\text{--}0.4$ .

### B. Large- and small-scale quadrant event contributions to the turbulent skin friction generation

The turbulent skin friction generation by the quadrant events is quantified using the method in Sec. III A. Figure 3 shows the premultiplied integrands groups  $(y/\delta) f_R^{Q,n}$  in (10), together with the corresponding skin friction coefficients in (11). Several characteristics are noted as follows: (i) The  $Q2$  and  $Q4$  integrands are responsible for the major part of  $C_f$ , equaling approximately 49% and 40%, respectively. Their maximums reside within the outer region  $y/\delta \simeq 0.3\text{--}0.4$ , consistent with the results shown in Fig. 2. In particular, the  $Q2$  contribution is roughly 20% higher than the  $Q4$  contribution. (ii) The  $Q1$  and  $Q3$  integrands are about half an order of magnitude lower than those of  $Q2$  and  $Q4$ , imply that the  $Q1$  and  $Q3$  events do not have a considerable impact on the  $C_f$ . Their negative contributions suggest that these quadrants diminish the mean skin friction generation. Comparing LB-05 and LB-08 with the DNS, at  $\text{Re}_\tau \simeq 500$ , most of the turbulent skin friction reduction is found in the  $Q2$  and  $Q4$  integrands at the outer region (i.e.,  $y/\delta > 0.1$ ). This provides evidence that the manipulation of the outer regions yields a significant amount of turbulent skin friction reduction, after accounting for the fact that the Reynolds number is low. For LB-01, as expected from the previous section, all the integrands increase in magnitude.

The turbulent skin friction generated by quadrant events with streamwise scales at a cutoff wavelength  $\lambda_{x,c} = 3\delta$  is explored through the premultiplied integrands groups (14), as shown in Fig. 4. For the DNS case shown, it reveals that the turbulent skin friction generated by  $Q1_L$  and  $Q3_L$  with streamwise scales  $\lambda_x > 3\delta$  is positive. The negative portions, as shown in Figs. 3(a) and 3(c), appear to be originated from the  $Q1_S$  and  $Q3_S$  with streamwise scales  $\lambda_x < 3\delta$  and their interaction components (i.e., denoted by LS and SL). Figures 4(c) and 4(d) further show that  $f_R^{LS,Q1} + f_R^{LS,Q3} = f_R^{LS,Q2} + f_R^{LS,Q4}$  and  $f_R^{SL,Q1} + f_R^{SL,Q3} = f_R^{SL,Q2} + f_R^{SL,Q4}$ , indicating that the quadrants interactions (LS and SL) do not have a direct impact on the  $C_{f,2}$  (i.e., in the mean sense). Through (15), this implies that the negative  $C_{f,2}$  generations are found to be the integrands  $f_R^{S,Q1}$  and  $f_R^{S,Q3}$ . Figures 4(a) and 4(b) also show that the  $f_R^{L,Q_n}$  and  $f_R^{S,Q_n}$  share a similarity for their peak locations and the overall shape at  $\text{Re}_\tau \simeq 500$  and  $\text{Re}_\tau \simeq 1000$  (DNS). They show a little Reynolds number dependence in that they all decrease with Reynolds numbers, which emphasizes the fact that the total  $C_f$  decreases with increasing Reynolds number. For LB-05 and LB-08 (note that the case LB-01 is excluded for brevity), the turbulent skin friction drag reductions are mainly due to the large-scale  $f_R^{L,Q2}$  and  $f_R^{L,Q4}$ , and the small-scale  $f_R^{S,Q2}$  and  $f_R^{S,Q4}$ . There are increases of  $f_R^{S,Q2}$  and  $f_R^{S,Q4}$  in the outer regions [as marked with two arrows in Fig. 4(b)] for LB-05 and LB-08, which presumably results from the manipulation of the large-scale motions that break up into small-scale motions, as previously discussed. The LB-05 and LB-08 collapse reasonably well to the DNS at  $\text{Re}_\tau \simeq 1000$ . These results are omitted for brevity. Table IV summarizes the turbulent skin friction generated by large- and small-scale quadrant events. For LB-05 and LB-08, the large- and small-scale ejection and sweeps events lead to a substantial amount of turbulent skin friction reduction. The differences in the values between the LEBU cases (LB-05 and LB-08) and DNS in the  $C_{f,2}^{L,Q2}$  and  $C_{f,2}^{L,Q4}$  are quite similar to that of  $C_{f,2}^{S,Q2}$  and  $C_{f,2}^{S,Q4}$ . In particular, the  $C_{f,2}^{L,Q2}$  and  $C_{f,2}^{L,Q4}$

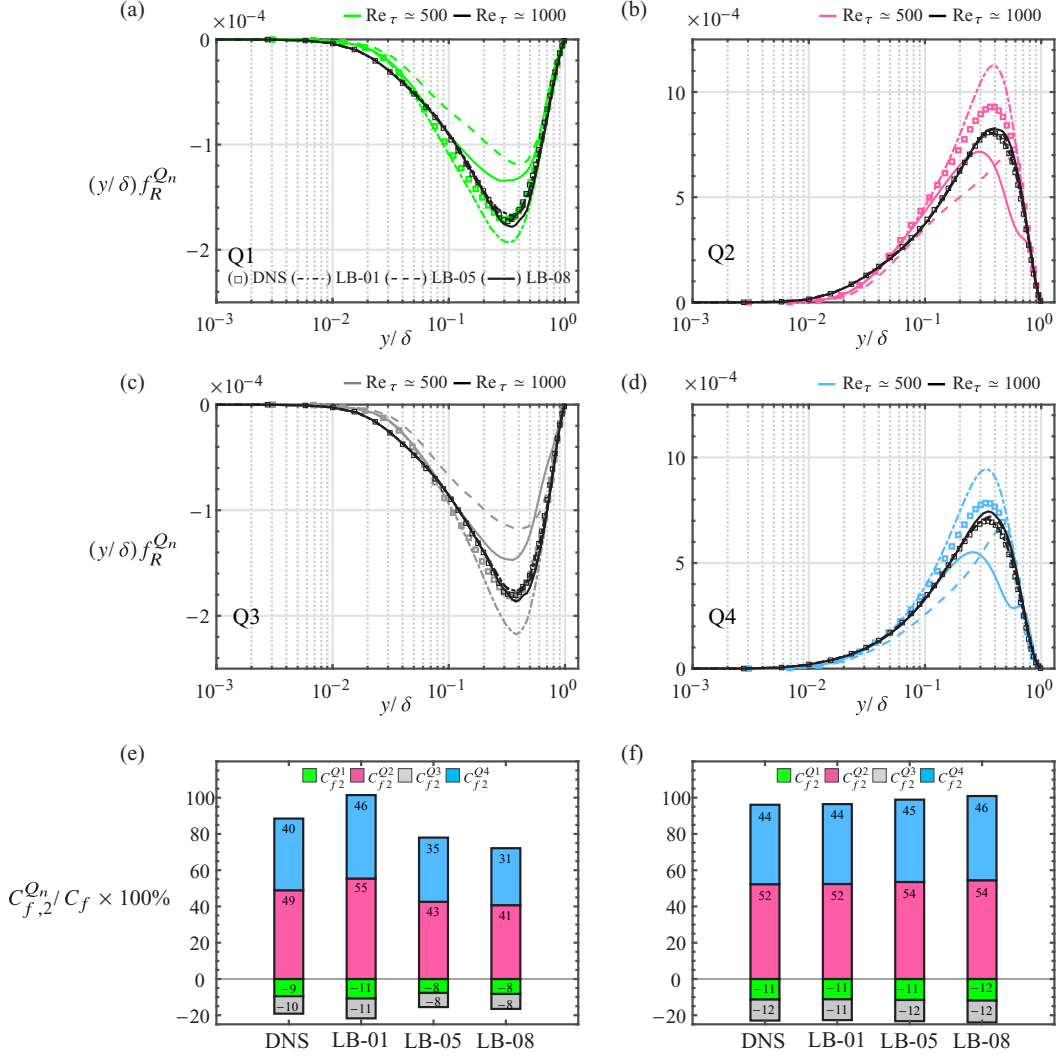


FIG. 3. Premultiplied integrands of each Reynolds shear stress quadrant based on (10): (a)  $(y/\delta)f_R^{Q1}$ , (b)  $(y/\delta)f_R^{Q2}$ , (c)  $(y/\delta)f_R^{Q3}$ , and (d)  $(y/\delta)f_R^{Q4}$ . Their percentage contributions based on (11) normalized by the total skin friction coefficient:  $C_{f,2}^{Qn}/C_f \times 100\%$  at (e)  $Re_\tau \simeq 500$  and (f)  $Re_\tau \simeq 1000$ .

TABLE IV. ( $\times 10^{-3}$ ) Contributions of large- and small-scale quadrant events to the total skin friction coefficient. The italicized numbers highlight the differences in the values between LB-05, LB-08 and DNS discussed in Sec. IV B.

| Case  | $Re_\tau$ | $C_{f,2}^{L,Q1}$ | $C_{f,2}^{L,Q2}$ | $C_{f,2}^{L,Q3}$ | $C_{f,2}^{L,Q4}$ | $C_{f,2}^{S,Q1}$ | $C_{f,2}^{S,Q2}$ | $C_{f,2}^{S,Q3}$ | $C_{f,2}^{S,Q4}$ |
|-------|-----------|------------------|------------------|------------------|------------------|------------------|------------------|------------------|------------------|
| LB-01 | 520       | 0.132            | 0.474            | 0.144            | 0.426            | -0.141           | 1.088            | -0.108           | 0.927            |
| LB-05 | 480       | 0.085            | <i>0.291</i>     | 0.088            | <i>0.257</i>     | -0.088           | <i>0.800</i>     | -0.071           | <i>0.682</i>     |
| LB-08 | 530       | 0.091            | <i>0.322</i>     | 0.099            | <i>0.272</i>     | -0.119           | <i>0.830</i>     | -0.086           | <i>0.664</i>     |
| DNS   | 520       | 0.121            | <i>0.442</i>     | 0.130            | <i>0.394</i>     | -0.126           | <i>0.980</i>     | -0.094           | <i>0.809</i>     |
|       | 990       | 0.104            | 0.328            | 0.117            | 0.294            | -0.145           | 0.945            | -0.120           | 0.801            |

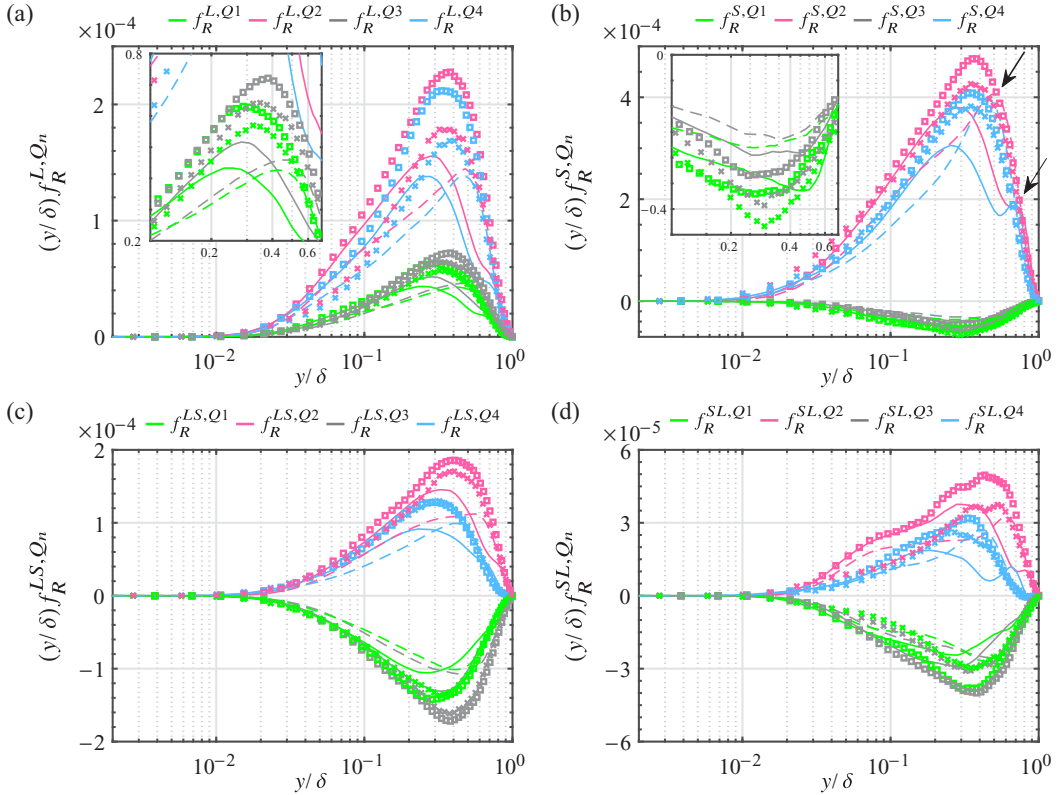


FIG. 4. Comparison of the premultiplied integrands (14) between DNS, LB-05, and LB-08. (a)  $(y/\delta)f_R^{L,Q_n}$ , (b)  $(y/\delta)f_R^{S,Q_n}$ , (c)  $(y/\delta)f_R^{LS,Q_n}$ , and (d)  $(y/\delta)f_R^{SL,Q_n}$ . Symbols and lines are DNS ( $\square$ ), LB-05 (---), and LB-08 (—) at  $Re_\tau \simeq 500$ , and DNS ( $\times$ ) at  $Re_\tau \simeq 1000$ . The arrows in (b) denote features discussed in the text.

associated with ejection and sweep events of streamwise scales  $\lambda_x > 3\delta$  are found to be reduced by 34% and 35% for LB-05, and 27% and 31% for LB-08, whereas the  $C_{f,2}^{S,Q_2}$  and  $C_{f,2}^{S,Q_4}$  associated with ejection and sweep events of streamwise scales  $\lambda_x < 3\delta$  are reduced by 18% and 16% for LB-05 and 15% and 18% for LB-08, as shown by the italicized values in Table IV. It could be concluded that a considerable portion of turbulent skin friction reduction as observed in LB-05 and LB-08 is by the inhibition of the sweep and ejection events at  $\lambda_x > 3\delta$ . The Reynolds number in the present study is moderate; it would be reasonable to conjecture that at sufficiently high Reynolds numbers, more attention should be focused on targeting these large-scale motions to achieve a desirable amount of skin friction reduction.

To quantify the degrees of turbulent skin friction generation with respect to the quadrant events, we define

$$R_{Q_n}^L = \frac{(C_{f,2}^{L,Q_n})_{\text{DNS}} - (C_{f,2}^{L,Q_n})_{\text{LB}}}{|(C_{f,2})_{\text{DNS}} - (C_{f,2})_{\text{LB}}|}, \quad R_{Q_n}^S = \frac{(C_{f,2}^{S,Q_n})_{\text{DNS}} - (C_{f,2}^{S,Q_n})_{\text{LB}}}{|(C_{f,2})_{\text{DNS}} - (C_{f,2})_{\text{LB}}|}, \quad (17)$$

which measures the total turbulent skin friction deviation with respect to that in the quadrant events. This infers that  $R > 0$  and  $R < 0$  correspond to inhibition and regeneration of quadrant events, respectively. Table V summarizes the values for  $Q_2$  and  $Q_4$  and Fig. 5 compares the values between all three LEBU cases. As for the LB-05 and LB-08, the values of  $R_{Q_2}^L$  and  $R_{Q_4}^L$  associated with the inhibition of large-scale ejection and sweep events are found to be similar to that of the small-scale  $R_{Q_2}^S$  and  $R_{Q_4}^S$ . This reinforces that a large amount of drag reduction could possibly be related to the

TABLE V. The sweep and ejection event contributions associated with the turbulent skin friction generation.

| Case  | $Re_\tau$ | $R_{Q2}^L$ | $R_{Q4}^L$ | $R_{Q2}^S$ | $R_{Q4}^S$ |
|-------|-----------|------------|------------|------------|------------|
| LB-01 | 520       | -0.1105    | -0.1136    | -0.3810    | -0.4169    |
| LB-05 | 480       | 0.2475     | 0.2230     | 0.2942     | 0.2067     |
| LB-08 | 530       | 0.2064     | 0.2077     | 0.2571     | 0.2490     |

inhibition of the large-scale sweep and ejection events for  $\lambda_x > 3\delta$ . On the other hand, for the LB-01 case shown, the values of  $R_{Q2}^S$  and  $R_{Q4}^S$  are larger than that of the  $R_{Q2}^L$  and  $R_{Q4}^L$ , suggesting that the regeneration of small-scale ejection and sweep events appears more prominent than the regeneration of large-scale ejection and sweep events  $\lambda_x > 3\delta$ ; however, the latter appears to be non-negligible.

## V. CONCLUSIONS

The skin friction coefficient modified by LEBUs placed at different distances from the wall has been investigated using the FIK-identity approach coupled with scale decomposition. The FIK-based scale decomposition shows that the large-scale motions at  $\lambda_x > 3\delta$  account for 27–29% of the total skin friction, which is comparable to previous studies for turbulent channels and boundary layer flows at relatively high Reynolds number [28,30]. A significant turbulent skin friction reduction in the LEBU flows was found in the large-scale turbulent skin friction, and part of the large-scale turbulent skin friction is redistributed to the small-scale counterparts, reflecting the break-up effect of large-scale momentum bulge into small-scale turbulence observed in the previous study [43]. The results further support that the LEBU device is effective for outer layer control in the turbulent boundary layer. Future studies can be focused on optimizing LEBU geometry to achieve the desired flow control characteristics.

A different method based on the FIK identity and quadrant analysis of Reynolds shear stress has been proposed. The method takes into consideration the quadrant events of Reynolds shear stress and their scale-by-scale contributions to turbulent skin friction. While this quantification has shown that the sweep and ejection events with streamwise scales of  $\lambda_x < 3\delta$  are responsible for the major part of the turbulent skin friction, it has emphasized the importance that the sweep and ejection

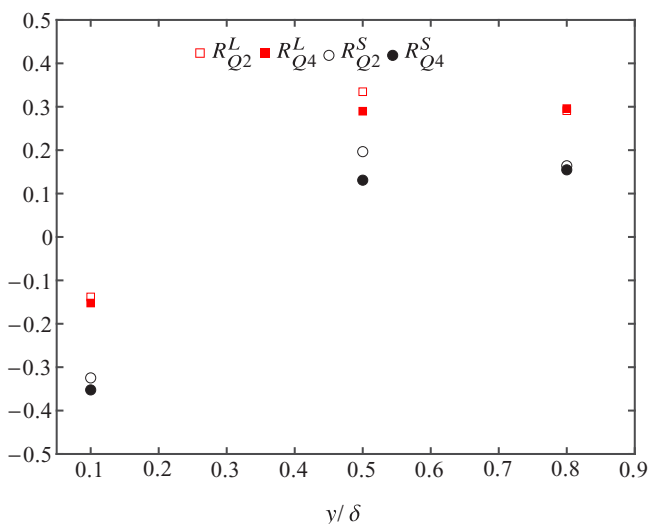


FIG. 5. Variations of attenuation and regeneration rates with wall-normal locations of LEBUs.

events with streamwise scale of  $\lambda_x > 3\delta$  are accounted for a considerable portion of turbulent skin friction, despite the moderate Reynolds number considered in the present study. The results have also revealed that the inhibition of sweep and ejection events with a streamwise scale of  $\lambda_x > 3\delta$  is directly associated with substantial turbulent skin friction reduction. Flow control targeting large-scale motions has been a recent subject of interest in developing flow control strategies. The present study might provide an alternative approach for quantifying the statistical contributions of the large- and small-scale sweep and ejection events to the skin friction.

### ACKNOWLEDGMENTS

This work was supported with supercomputing resources provided by the Phoenix HPC service at the University of Adelaide. This research was also undertaken with the assistance of resources provided at the NCI NF through the National Computational Merit Allocation Scheme, supported by the Australian Government. This work was supported by resources provided by the Pawsey Supercomputing Centre with funding from the Australian Government and the Government of Western Australia. The simulations were performed on resources provided by the Swedish National Infrastructure for Computing (SNIC) at the PDC Center for High Performance Computing at KTH, Stockholm. Financial support from the Australian Research Council, the Lundequvist Foundation, and the Knut and Alice Wallenberg Foundation is gratefully acknowledged.

### APPENDIX: SCALE DECOMPOSITION OF REYNOLDS STRESS

The flow fields obtained from time series data can be expressed with a superposition of some spatial or temporal coefficients and Fourier modes such that [57]

$$u_i(\mathbf{x}, t) = u_i^L(k_m, \mathbf{x}, t) + u_i^S(k_m, \mathbf{x}, t), \quad (\text{A1})$$

for an arbitrary but finite cutoff wave number (or frequency)  $k_m$  such that  $|K| > |k_m| > 0$ . The wave-number range  $k$  is such that  $|K| > |k| > |k_m|$  corresponds to  $u_i^S$  and  $|k_m| \geq |k| \geq 0$  corresponds to  $u_i^L$ . The velocity products  $u_i u_j$  are collected and arranged into the matrix form, which can be expressed as

$$u_i u_j = \mathbf{M}^L + \mathbf{M}^S + \mathbf{M}^{LS} + \mathbf{M}^{SL}, \quad (\text{A2})$$

where  $\mathbf{M}^L = \mathbf{M}^L(k_m, \mathbf{x}, t)$ . The spanwise and temporal-averaged velocity products (correlations)  $\langle u_i^L u_j^L \rangle$  at a streamwise location  $x$  are the correlation matrix  $\langle \mathbf{M}^L \rangle$  with finite wave-number leading order  $|K| > |k|$  in the form of

$$\langle \mathbf{M}^L \rangle(k, y) = \begin{bmatrix} \langle M_{1,1}^L \rangle & \cdots & \langle M_{1,n}^L \rangle & \cdots & \cdots \\ \langle M_{2,1}^L \rangle & \cdots & \langle M_{2,n}^L \rangle & \cdots & \cdots \\ \vdots & \vdots & \ddots & \vdots & \vdots \\ \langle M_{m,1}^L \rangle & \cdots & \langle M_{m,n}^L \rangle & \cdots & \cdots \\ \cdots & \cdots & \cdots & \cdots & \cdots \end{bmatrix}, \quad (\text{A3})$$

where  $\langle M_{m,n}^L \rangle = \langle u_i^L u_j^L \rangle(k_m, y_n)$ ,  $|K| > |k_m| = |m\Delta k|$ , and  $\delta > y_n = n\Delta y$ . The correlation term is  $\langle M_{m,n}^L \rangle = \int_0^{k_m} \Phi_{u_i u_j}(k, y_n) dk$ . Therefore, the co-spectrum can be approximated by the leading-order

wave-number differentiated matrix  $\langle \dot{\mathbf{M}}^L \rangle$ ,

$$\Phi_{u_i u_j}(k, y) = \langle \dot{\mathbf{M}}^L(k, y) \rangle = \begin{bmatrix} \langle \dot{M}_{1,1}^L \rangle & \dots & \langle \dot{M}_{1,n}^L \rangle & \dots & \dots \\ \langle \dot{M}_{2,1}^L \rangle & \dots & \langle \dot{M}_{2,n}^L \rangle & \dots & \dots \\ \vdots & \vdots & \ddots & \vdots & \vdots \\ \langle \dot{M}_{m,1}^L \rangle & \dots & \langle \dot{M}_{m,n}^L \rangle & \dots & \dots \\ \dots & \dots & \dots & \dots & \dots \end{bmatrix}, \quad (\text{A4})$$

where  $\langle \dot{M}_{m,n}^L \rangle = \langle u_i^L u_j^L \rangle_{k_m, y_n}$  can be approximated by the central differences and retains only the leading-order terms to obtain

$$\begin{aligned} \langle \dot{M}_{m,n}^L \rangle &= \langle u_i^L u_j^L \rangle_{k_m, y_n} = \frac{1}{2\Delta k} [\langle M_{m+1,n}^L \rangle - \langle M_{m-1,n}^L \rangle] + O(\Delta k^2) \\ &\sim \frac{1}{2\Delta k} [\langle M_{m+1,n}^L \rangle - \langle M_{m-1,n}^L \rangle], \end{aligned} \quad (\text{A5})$$

with  $\langle M_{0,n}^L \rangle = 0$  and  $\langle M_{K,n}^L \rangle \simeq \langle u_i u_j \rangle$ . Considering (A2), we take a spanwise and temporal average and obtain that

$$\langle u_i u_j \rangle = \langle \mathbf{M}^L \rangle + \langle \mathbf{M}^S \rangle, \quad (\text{A6})$$

where the cross correlations  $\langle \mathbf{M}^{LS} \rangle$  and  $\langle \mathbf{M}^{SL} \rangle$  are zero [57]. Differentiating with respect to wave number gives

$$\langle \dot{\mathbf{M}}^S(k, y) \rangle = -\langle \dot{\mathbf{M}}^L(k, y) \rangle = -\Phi_{u_i u_j}(k, y). \quad (\text{A7})$$

- 
- [1] J. Kim, P. Moin, and R. Moser, Turbulence statistics in fully developed channel flow at low Reynolds number, *J. Fluid Mech.* **177**, 133 (1987).
- [2] J. Jeong, F. Hussain, W. Schoppa, and J. Kim, Coherent structures near the wall in a turbulent channel flow, *J. Fluid Mech.* **332**, 185 (1997).
- [3] S. J. Kline, W. C. Reynolds, F. A. Schraub, and P. W. Runstadler, The structure of turbulent boundary layers, *J. Fluid Mech.* **30**, 741 (1967).
- [4] E. R. Corino and R. S. Brodkey, A visual investigation of the wall region in turbulent flow, *J. Fluid Mech.* **37**, 1 (1969).
- [5] H. T. Kim, S. J. Kline, and W. C. Reynolds, The production of turbulence near a smooth wall in a turbulent boundary layer, *J. Fluid Mech.* **50**, 133 (1971).
- [6] J. M. Hamilton, J. Kim, and F. Waleffe, Regeneration mechanisms of near-wall turbulence structures, *J. Fluid Mech.* **287**, 317 (1995).
- [7] W. Schoppa and F. Hussain, Coherent structure generation in near-wall turbulence, *J. Fluid Mech.* **453**, 57 (2002).
- [8] S. Discetti, G. Bellani, R. Örlü, J. Serpieri, C. S. Vila, M. Raiola, X. Zheng, L. Mascotelli, A. Talamelli, and A. Ianiro, Characterization of very-large-scale motions in high-Re pipe flows, *Expt. Therm. Fluid Sci.* **104**, 1 (2019).
- [9] S. S. Lu and W. W. Willmarth, Measurements of the structure of the Reynolds stress in a turbulent boundary layer, *J. Fluid Mech.* **60**, 481 (1973).
- [10] K. C. Kim and R. J. Adrian, Very large-scale motion in the outer layer, *Phys. Fluids* **11**, 417 (1999).
- [11] J. C. del Álamo and J. Jiménez, Spectra of the very large anisotropic scales in turbulent channels, *Phys. Fluids* **15**, L41 (2003).



- [12] J. B. Anders, J. N. Hefner, and D. M. Bushnell, Performance of large-eddy breakup devices at post-transitional Reynolds numbers, 22nd Aerospace Sciences Meeting, *AIAA J.* (1984).
- [13] C. D. Tomkins and R. J. Adrian, Spanwise structure and scale growth in turbulent boundary layers, *J. Fluid Mech.* **490**, 37 (2003).
- [14] N. Hutchins and I. Marusic, Evidence of very long meandering features in the logarithmic region of turbulent boundary layers, *J. Fluid Mech.* **579**, 1 (2007).
- [15] M. Guala, S. E. Himmema, and R. J. Adrian, Large-scale and very-large-scale motions in turbulent pipe flow, *J. Fluid Mech.* **554**, 521 (2006).
- [16] B. Balakumar and R. Adrian, Large- and very-large-scale motions in channel and boundary-layer flows, *Philos. Trans. R. Soc. Lond. A* **365**, 665 (2007).
- [17] N. Hutchins and I. Marusic, Large-scale influences in near-wall turbulence, *Philos. Trans. R. Soc. Lond. A* **365**, 647 (2007).
- [18] R. Mathis, N. Hutchins, and I. Marusic, Large-scale amplitude modulation of the small-scale structures in turbulent boundary layers, *J. Fluid Mech.* **628**, 311 (2009).
- [19] H. Abe, H. Kawamura, and H. Choi, Very large-scale structures and their effects on the wall shear-stress fluctuations in a turbulent channel flow up to  $Re_\tau \approx 640$ , *J. Fluids Eng.* **126**, 835 (2004).
- [20] R. Örlü and P. Schlatter, On the fluctuating wall-shear stress in zero pressure-gradient turbulent boundary layer flows, *Phys. Fluids* **23**, 021704 (2011).
- [21] Y. Hwang, Near-wall turbulent fluctuations in the absence of wide outer motions, *J. Fluid Mech.* **723**, 264 (2013).
- [22] K. Fukagata, K. Iwamoto, and N. Kasagi, Contribution of Reynolds stress distribution to the skin friction in wall-bounded flows, *Phys. Fluids* **14**, L73 (2002).
- [23] N. Renard and S. Deck, A theoretical decomposition of mean skin friction generation into physical phenomena across the boundary layer, *J. Fluid Mech.* **790**, 339 (2016).
- [24] M. Yoon, J. Ahn, J. Hwang, and H. J. Sung, Contribution of velocity-vorticity correlations to the frictional drag in wall-bounded turbulent flows, *Phys. Fluids* **28**, 081702 (2016).
- [25] R. J. Adrian, C. D. Meinhart, and C. D. Tomkins, Vortex organization in the outer region of the turbulent boundary layer, *J. Fluid Mech.* **422**, 1 (2000).
- [26] C. Chin, J. Philip, J. Klewicki, A. Ooi, and I. Marusic, Reynolds-number-dependent turbulent inertia and onset of log region in pipe flows, *J. Fluid Mech.* **757**, 747 (2014).
- [27] M. Yoon, J. Hwang, and H. J. Sung, Contribution of large-scale motions to the skin friction in a moderate adverse pressure gradient turbulent boundary layer, *J. Fluid Mech.* **848**, 288 (2018).
- [28] S. Deck, N. Renard, R. Laraufie, and P.-É. Weiss, Large-scale contribution to mean wall shear stress in high-Reynolds-number flat-plate boundary layers up to  $Re_\theta = 13650$ , *J. Fluid Mech.* **743**, 202 (2014).
- [29] Y. Duan, Q. Zhong, G. Wang, P. Zhang, and D. Li, Contributions of different scales of turbulent motions to the mean wall-shear stress in open channel flows at low-to-moderate Reynolds numbers, *J. Fluid Mech.* **918**, A40 (2021).
- [30] M. de Giovanetti, Y. Hwang, and H. Choi, Skin-friction generation by attached eddies in turbulent channel flow, *J. Fluid Mech.* **808**, 511 (2016).
- [31] J.-S. Kim, J. Hwang, M. Yoon, J. Ahn, and H. J. Sung, Influence of a large-eddy breakup device on the frictional drag in a turbulent boundary layer, *Phys. Fluids* **29**, 065103 (2017).
- [32] I. C. Chan, R. Örlü, P. Schlatter, and R. C. Chin, The skin-friction coefficient of a turbulent boundary layer modified by a large-eddy break-up device, *Phys. Fluids* **33**, 035153 (2021).
- [33] R. J. Adrian, Hairpin vortex organization in wall turbulence, *Phys. Fluids* **19**, 041301 (2007).
- [34] A. Lozano-Durán, O. Flores, and J. Jiménez, The three-dimensional structure of momentum transfer in turbulent channels, *J. Fluid Mech.* **694**, 100 (2012).
- [35] A. Lozano-Durán and J. Jiménez, Time-resolved evolution of coherent structures in turbulent channels: characterization of eddies and cascades, *J. Fluid Mech.* **759**, 432 (2014).
- [36] D. Fiscaletti, R. de Kat, and B. Ganapathisubramani, Spatial-spectral characteristics of momentum transport in a turbulent boundary layer, *J. Fluid Mech.* **836**, 599 (2018).
- [37] T. C. Corke, H. M. Nagib, and Y. Guezennec, A new view on origin, role and manipulation of large scales in turbulent boundary layers, NASA CR, Report No. 165861 (1982).

- [38] P. H. Alfredsson and R. Örlü, Large-eddy breakup devices—A 40 years perspective from a Stockholm horizon, *Flow, Turbul. Combust.* **100**, 877 (2018).
- [39] T. C. Corke, Y. Guezennic, and H. M. Nagib, Modification in drag of turbulent boundary layers resulting from manipulation of large-scale structures, *Viscous Flow Drag Reduction*, *Prog. Astronaut Aeromot.* **72**, 128 (1979).
- [40] J. B. Anders, Boundary layer manipulators at high Reynolds numbers, in *Structure of Turbulence and Drag Reduction*, edited by A. Gyr (Springer, Berlin, 1990), pp. 475–482.
- [41] A. Sahlin, A. V. Johansson, and P. H. Alfredsson, The possibility of drag reduction by outer layer manipulators in turbulent boundary layers, *Phys. Fluids* **31**, 2814 (1988).
- [42] P. Spalart, M. Strelets, and A. Travin, Direct numerical simulation of large-eddy-break-up devices in a boundary layer, *Intl. J. Heat Fluid Flow* **27**, 902 (2006).
- [43] C. Chin, R. Örlü, J. Monty, N. Hutchins, A. Ooi, and P. Schlatter, Simulation of a large-eddy-break-up device (LEBU) in a moderate Reynolds number turbulent boundary layer, *Flow Turbul. Combust.* **98**, 445 (2017).
- [44] A. E. Smith and S. Gordeyev, Aero-optical mitigation of turbulent boundary layers using large-eddy break-up devices, in *AIAA Paper 2014-0321* (American Institute of Aeronautics and Astronautics, 2014).
- [45] M. Chevalier, A. Lundbladh, and D. S. Henningson, SIMSON—A pseudo-spectral solver for incompressible boundary layer flow, Tech. Rep. TRITA-MEK 2007:07 (KTH Mechanics, Stockholm, Sweden, 2007).
- [46] Q. Li, P. Schlatter, and D. S. Henningson, Spectral simulations of wall-bounded flows on massively parallel computers, Tech. Rep. KTH Mechanics, Stockholm, Sweden. In Licentiate Thesis of Q. Li, 2009 (KTH Mechanics, Stockholm, Sweden, 2008).
- [47] S. Stolz, N. A. Adams, and L. Kleiser, An approximate deconvolution model for large-eddy simulation with application to incompressible wall-bounded flows, *Phys. Fluids* **13**, 997 (2001).
- [48] P. Schlatter, S. Stolz, and L. Kleiser, LES of transitional flows using the approximate deconvolution model, *Intl. J. Heat Fluid Flow* **25**, 549 (2004).
- [49] P. Schlatter and R. Örlü, Turbulent boundary layers at moderate Reynolds numbers: Inflow length and tripping effects, *J. Fluid Mech.* **710**, 5 (2012).
- [50] P. Schlatter and R. Örlü, Assessment of direct numerical simulation data of turbulent boundary layers, *J. Fluid Mech.* **659**, 116 (2010).
- [51] D. Goldstein, R. Handler, and L. Sirovich, Modeling a no-slip flow boundary with an external force field, *J. Comput. Phys.* **105**, 354 (1993).
- [52] C. I. Chan, P. Schlatter, and R. C. Chin, Interscale transport mechanisms in turbulent boundary layers, *J. Fluid Mech.* **921**, A13 (2021).
- [53] J. C. del Álamo and J. Jiménez, Estimation of turbulent convection velocities and corrections to Taylor’s approximation, *J. Fluid Mech.* **640**, 5 (2009).
- [54] M. Samie, W. Baars, A. Rouhi, P. Schlatter, R. Örlü, I. Marusic, and N. Hutchins, Near wall coherence in wall-bounded flows and implications for flow control, *Intl. J. Heat Fluid Flow* **86**, 108683 (2020).
- [55] J. M. Wallace, Quadrant analysis in turbulence research: History and evolution, *Annu. Rev. Fluid Mech.* **48**, 131 (2016).
- [56] C. D. Tomkins and R. J. Adrian, Energetic spanwise modes in the logarithmic layer of a turbulent boundary layer, *J. Fluid Mech.* **545**, 141 (2005).
- [57] T. Kawata and P. H. Alfredsson, Inverse Interscale Transport of the Reynolds Shear Stress in Plane Couette Turbulence, *Phys. Rev. Lett.* **120**, 244501 (2018).